Windowed Radon Transform and Tensor Rank-1 Decomposition for Adaptive Beamforming in Ultrafast Ultrasound

Samuel Beuret [1] and Jean-Philippe Thiran [2]

[1]Swiss Federal Institute of Technology in Lausanne (EPFL)
[2]Affiliation not available

October 30, 2023

Abstract

Ultrafast ultrasound has recently emerged as an alternative to traditional focused ultrasound. By virtue of the low number of insonifications it requires, ultrafast ultrasound enables the imaging of the human body at potentially very high frame rates. However, unaccounted for speed-of-sound variations in the insonified medium often result in phase aberrations in the reconstructed images. The diagnosis capability of ultrafast ultrasound is thus ultimately impeded. Therefore, there is a strong need for adaptive beamforming methods that are resilient to speed-of-sound aberrations. Several of such techniques have been proposed recently but they often lack parallelizability or the ability to directly correct both transmit and receive phase aberrations. In this article, we introduce an adaptive beamforming method designed to address these shortcomings. To do so, we compute the windowed Radon transform of several complex radio-frequency images reconstructed using delay-and-sum. Then, we apply to the obtained local sinograms weighted tensor rank-1 decompositions and their results are eventually used to reconstruct a corrected image. We demonstrate using simulated data that our method is able to successfully recover aberration-free images and that it outperforms both coherent compounding and the recently introduced SVD beamformer. Finally, we validate the proposed beamforming technique on in-vivo data, resulting in a significant improvement of image quality compared to the two reference methods.

Windowed Radon Transform and Tensor Rank-1 Decomposition for Adaptive Beamforming in Ultrafast Ultrasound

Samuel Beuret, *Student Member, IEEE* and Jean-Philippe Thiran, *Member, IEEE*

***Abstract*— Ultrafast ultrasound has recently emerged as an alternative to traditional focused ultrasound. By virtue of the low number of insonifications it requires, ultrafast ultrasound enables the imaging of the human body at potentially very high frame rates. However, unaccounted for speed-of-sound variations in the insonified medium often result in phase aberrations in the reconstructed images. The diagnosis capability of ultrafast ultrasound is thus ultimately impeded. Therefore, there is a strong need for adaptive beamforming methods that are resilient to speed-of-sound aberrations. Several of such techniques have been proposed recently but they often lack parallelizability or the ability to directly correct both transmit and receive phase aberrations. In this article, we introduce an adaptive beamforming method designed to address these shortcomings. To do so, we compute the windowed Radon transform of several complex radio-frequency images reconstructed using delay-and-sum. Then, we apply to the obtained local sinograms weighted tensor rank-1 decompositions and their results are eventually used to reconstruct a corrected image. We demonstrate using simulated data that our method is able to successfully recover aberration-free images and that it outperforms both coherent compounding and the recently introduced SVD beamformer. Finally, we validate the proposed beamforming technique on in-vivo data, resulting in a significant improvement of image quality compared to the two reference methods.**

***Index Terms*— Aberration Correction, Adaptive Beamforming, Ultrafast Ultrasound**

I. Introduction

In the last 20 years, ultrafast ultrasound has emerged as a new paradigm rivalling traditional focused ultrasound [1]. It relies on the emission of unfocused waves by an ultrasound transducer. The recorded echoes are then synthetically focused to recover an image estimating the reflectivity of the human soft tissues. To improve the image quality, images corresponding to different insonifications can then be combined into one, most commonly using coherent compounding [2]. Due to the high frame-rate the method allows, ultrafast ultrasound has enabled new diagnostic techniques such as shear-waves elastography [3]–[5] or neurofunctional imaging [6], among others.

Paper submitted for reviews on December 30th 2022.

Samuel Beuret and Jean-Philippe Thiran are with the Signal Processing Laboratory 5 at the École polytechnique fédérale de Lausanne (EPFL), Lausanne, Switzerland (e-mails: samuel.beuret@epfl.ch, jean-philippe.thiran@epfl.ch).

Jean-Philippe Thiran is also with the Department of Radiology, University Hospital Center and University of Lausanne, Lausanne, Switzerland.

To reconstruct an image, ultrafast ultrasound—as well as traditional focused ultrasound—presupposes a constant speed of sound (SoS) in the imaged tissues. This hypothesis is however not met in practice since the SoS of human soft tissues can vary up to the order of 5% [7]. In effect, SoS variations introduce high-order aberrations in the reconstructed images that are ultimately detrimental to the diagnostic capability of ultrasound imaging [8], [9]. Therefore, there exists a strong impetus to design image reconstruction techniques that are resilient to aberrations induced by SoS variations.

Numerous aberration correction methods have thus been proposed throughout the development of ultrasound imaging [10]–[12]. A large part of these methods posits the existence of a thin aberrating layer in front of the transducer. Angular aberrations are therefore supposed constant in the medium. This hypothesis is justified in specific imaging configurations. In general, however, such methods fail to address the aberrations generated by a spatially varying SoS distribution.

The recent years have witnessed the development of pulse-echo SoS imaging methods [13]–[16]. Their goal is to reconstruct a map of the local SoS from pulse-echo ultrasound measurements. To correct for SoS aberrations, propagation delays can be deduced from the imaged SoS and then used by delay-and-sum (DAS) and coherent compounding to reconstruct an image [17], [18]. Especially relevant to our work is the method presented in [19], where directional filters applied to beamformed images are used to take into account aberrations. Several drawbacks of this general approach can however be highlighted. First, the local SoS recovery currently lacks robustness, which may lead to errors in the propagation delays estimation. Second, such techniques are also computationally heavy and inherently non-parralelizable due to the SoS map reconstruction. Finally, such methods do not allow a gain of performance compared to DAS in the absence of aberrations.

In contrast, novel approaches have emerged recently to better exploit the coherence existing between insonifications. These methods provide an increased robustness against SoS aberrations along with other artifacts such as diffraction artefacts (side lobes, grating lobes) and multiple scattering artefacts. The SVD beamformer introduced in [20], [21] is especially relevant to our work. Its basic principle is to beamform using DAS a series of complex radio-frequency (CRF) images—one per insonification—and extract patches from them. A stack of patches can be interpreted as a matrix and its leading right singular vector corresponds to a patch

of the corrected image. In addition, the leading left singular vector corresponds to local aberrations and can be used to estimate local SoS [22]. Computationally light and easily parralelizable, SVD beamforming is however only able to directly correct for transmit (Tx) aberrations. Receive (Rx) aberrations are overlooked, penalizing in practice the performances of the method. Another proposed approach exploiting redundancy between insonifications is ultrasound matrix imaging (UMI) [23], [24]. This technique constructs virtual emitters and receivers in the imaged medium. Aberration correction—among other features of UMI—is performed by maximizing the energy of emitters-receivers pairs when placed at the same location. However, UMI-based aberration correction is computationally demanding and unfit to parralelization since several image correction steps are necessary.

Therefore, our goal in this article is to propose an adaptive beamforming method for ultrafast ultrasound that adheres to the following guidelines:

- It should be able to simultaneously correct for spatially-varying Tx and Rx phase aberrations,
- It should also provide additional robustness to artifacts such as multiple scattering and diffraction artifacts with respect to coherent compounding,
- It should be easily parallelizable and thus avoid to iteratively reconstruct images or to compute a local SoS map.

To do so, we rely on the concept of change of basis from the canonical sensor basis to a Rx plane waves (PWs) basis—sometimes denoted as Radon domain—proposed recently [25], [26]. Following [20], [24], the main rationale behind the proposed method is to express the data into a local Rx PW basis to account for the locality of the phase aberrations induced by SoS variations.

II. Theory

In this section, we first describe the model of the received signal. Then, we detail the theoretical argument underpinning the proposed method.

A. Signal Model and Beamforming

In this article, we restrict ourselves to the case of a linear transducer. We suppose that it is aligned with the x axis and facing the positive z direction. An element of the transducer is then defined by its position $\boldsymbol{r}^{\mathrm{el}} = [x^{\mathrm{el}}, 0]^T$. Furthermore, we assume that the transducer emits PWs parametrized by their steering angles θ^{Tx}. According to [27], we model the CRF echo-signal m received by an arbitrary sensor when an arbitrary steered PW is transmitted as

$$m\left(\theta^{\mathrm{Tx}}, x^{\mathrm{el}}, t\right) = v_{\mathrm{pe}}(t) *_t \int_{\boldsymbol{r}} \left[\tilde{h}^{\mathrm{Tx}}\left(\theta^{\mathrm{Tx}}, \boldsymbol{r}, t\right) *_t \tilde{h}^{\mathrm{Rx}}\left(x^{\mathrm{el}}, \boldsymbol{r}, t\right)\right] \gamma(\boldsymbol{r})\, \mathrm{d}\boldsymbol{r}, \quad (1)$$

where the functions $\tilde{h}^{\mathrm{Tx}}$ and $\tilde{h}^{\mathrm{Rx}}$ designate the Tx and Rx spatial impulse responses (SIRs), respectively, and $*_t$ represents a temporal convolution. We denote by v_{pe} the pulse-echo waveform accounting for the electro-acoustic (Tx) impulse response, acousto-electric (Rx) impulse response and electric excitation waveform. We represent by γ the tissue reflectivity function (TRF) which factors in the local fluctuations of density and SoS generating scattered echo signals.

Following [28], [29], we introduce a Tx and Rx far-field approximations. Moreover, we assume that v_{pe} is a complex signal with center frequency $f_0 = \omega_0/2\pi$. Under these assumption, we can rewrite (1) as

$$m\left(\theta^{\mathrm{Tx}}, x^{\mathrm{el}}, t\right) = \int_{\boldsymbol{r}} h^{\mathrm{Tx}}\left(\theta^{\mathrm{Tx}}, \boldsymbol{r}\right)\, h^{\mathrm{Rx}}\left(x^{\mathrm{el}}, \boldsymbol{r}\right) e^{-j\omega_0 \Delta\tau^{\mathrm{Tx}}\left(\theta^{\mathrm{Tx}}, \boldsymbol{r}\right)} e^{-j\omega_0 \Delta\tau^{\mathrm{Rx}}\left(x^{\mathrm{el}}, \boldsymbol{r}\right)} v_{\mathrm{pe}}\Big(t - \tau^{\mathrm{Tx}}\left(\theta^{\mathrm{Tx}}, \boldsymbol{r}\right) - \tau^{\mathrm{Rx}}\left(x^{\mathrm{el}}, \boldsymbol{r}\right)\Big) \gamma(\boldsymbol{r})\, \mathrm{d}\boldsymbol{r}. \quad (2)$$

Here, the functions h^{Tx} and h^{Rx} are real and positive and they factor in element directivity, decay and attenuation. In (2), we split the Tx and Rx propagation times into two distinct terms: the expected propagation times τ^{Tx}, τ^{Rx} and the aberrations delays $\Delta\tau^{\mathrm{Tx}}$, $\Delta\tau^{\mathrm{Rx}}$. In-line with previous works on SoS estimation and aberration correction [15], [19], [20], we reduce the effect of aberration delay to a phase shift by assuming that v_{pe} is narrow-band.

We compute the expected propagation times by positing a uniform SoS c_0 in the medium. The Tx propagation time is then given by

$$\tau^{\mathrm{Tx}}\left(\theta^{\mathrm{Tx}}, \boldsymbol{r}\right) = \frac{1}{c_0}\left\langle \boldsymbol{u}\left(\theta^{\mathrm{Tx}}\right), \boldsymbol{r}\right\rangle, \text{ with } \boldsymbol{u}(\theta) = \begin{bmatrix}\sin(\theta)\\ \cos(\theta)\end{bmatrix}, \quad (3)$$

and the Rx propagation time is given by

$$\tau^{\mathrm{Rx}}\left(x^{\mathrm{el}}, \boldsymbol{r}\right) = \frac{1}{c_0}\|\boldsymbol{r} - \boldsymbol{r}^{\mathrm{el}}\|_2. \quad (4)$$

Aberration delays $\Delta\tau^{\mathrm{Tx/Rx}}$ are therefore the result of a mismatch between the physical local SoS and the assumed SoS c_0.

We now suppose that DAS is applied independently to the data obtained for each PW insonification. Moreover, we assume that we have access to a continuous range of sensor positions $x^{\mathrm{el}} \in \left[-x^{\max}, x^{\max}\right]$. Under this hypothesis, DAS can be expressed as

$$\gamma^{\mathrm{DAS}}\left(\theta^{\mathrm{Tx}}, \boldsymbol{r}'\right) = \int_{x^{\mathrm{el}}=-x^{\max}}^{x^{\max}} a^{\mathrm{Tx}}\left(\theta^{\mathrm{Tx}}, \boldsymbol{r}'\right)\, a^{\mathrm{Rx}}\left(x^{\mathrm{el}}, \boldsymbol{r}'\right) m\Big(\theta^{\mathrm{Tx}}, x^{\mathrm{el}}, \tau^{\mathrm{Tx}}\left(\theta^{\mathrm{Tx}}, \boldsymbol{r}'\right) + \tau^{\mathrm{Rx}}\left(x^{\mathrm{el}}, \boldsymbol{r}'\right)\Big)\, \mathrm{d}\boldsymbol{r}, \quad (5)$$

where a^{Tx} and a^{Rx} denote real and positive apodization weights. In particular, the sensor continuum hypothesis has the practical effect of neglecting grating lobes altogether. The resulting expression γ^{DAS} is a function of both the spatial position in the image $\boldsymbol{r}'$ and the Tx angle θ^{Tx}.

B. Local Angular Framework

To further our analysis, we focus on the vicinity $\mathbb{V}(\boldsymbol{r}^{\mathrm{w}})$ of a point $\boldsymbol{r}^{\mathrm{w}} = [x^{\mathrm{w}}, z^{\mathrm{w}}]^T$ in the image series γ^{DAS}. We first suppose that $a^{\mathrm{Tx/Rx}}$, $h^{\mathrm{Tx/Rx}}$, and $\Delta\tau^{\mathrm{Tx/Rx}}$ vary slowly in the medium and thus can be assumed constant in $\mathbb{V}(\boldsymbol{r}^{\mathrm{w}})$ and equal to their value at $\boldsymbol{r}^{\mathrm{w}}$. Practically, $\mathbb{V}(\boldsymbol{r}^{\mathrm{w}})$ is equivalent to the

isoplanatic patch used in [20], [23]. Moreover, we introduce a local Rx angle

$$\theta^{\mathrm{Rx}} = \arctan\left(\frac{x^{\mathrm{w}} - x^{\mathrm{el}}}{z^{\mathrm{w}}}\right), \tag{6}$$

and re-express each function of x^{el} as a function of θ^{Rx}. Based on this change of variable, we posit that the Rx expected time can be assumed linear within $\mathbb{V}(\boldsymbol{r}^{\mathrm{w}})$ and expressed as:

$$\tau^{\mathrm{Rx}}(\theta^{\mathrm{Rx}}, \boldsymbol{r}) \approx \frac{1}{c_0}\left\langle \boldsymbol{u}(\theta^{\mathrm{Rx}}), \boldsymbol{r} - \boldsymbol{r}^{\mathrm{w}}\right\rangle + \frac{z^{\mathrm{w}}}{c_0 \cos\left(\theta^{\mathrm{Rx}}\right)} \tag{7}$$

with $\boldsymbol{u}(\theta)$ the vector defined in (3). Factoring in (2), we can rewrite (5) as:

$$\gamma^{\mathrm{DAS}}(\theta^{\mathrm{Tx}}, \boldsymbol{r}') \approx \int_{\theta^{\mathrm{Rx}}} l^{\mathrm{Tx}}(\theta^{\mathrm{Tx}}) l^{\mathrm{Rx}}(\theta^{\mathrm{Rx}}) \int_{\boldsymbol{r}} \gamma(\boldsymbol{r}) \\ v_{\mathrm{pe}}\left(\frac{2}{c_0}\cos\left(\frac{\theta^{\mathrm{Tx}} - \theta^{\mathrm{Rx}}}{2}\right)\left\langle \boldsymbol{u}\left(\frac{\theta^{\mathrm{Tx}} + \theta^{\mathrm{Rx}}}{2}\right), \boldsymbol{r}' - \boldsymbol{r}\right\rangle\right) \mathrm{d}\boldsymbol{r}\, \mathrm{d}\theta^{\mathrm{Rx}}, \tag{8}$$

where we define two apodization/aberration functions

$$l^{\mathrm{Tx}}(\theta^{\mathrm{Tx}}) = a^{\mathrm{Tx}}(\theta^{\mathrm{Tx}}) h^{\mathrm{Tx}}(\theta^{\mathrm{Tx}}) e^{-j\omega_0 \Delta\tau^{\mathrm{Tx}}(\theta^{\mathrm{Tx}})}, \\ l^{\mathrm{Rx}}(\theta^{\mathrm{Rx}}) = \frac{z^{\mathrm{p}}}{\cos^2\left(\theta^{\mathrm{Rx}}\right)} a^{\mathrm{Rx}}(\theta^{\mathrm{Rx}}) h^{\mathrm{Rx}}(\theta^{\mathrm{Rx}}) e^{-j\omega_0 \Delta\tau^{\mathrm{Rx}}(\theta^{\mathrm{Rx}})}. \tag{9}$$

Note that there is an implicit dependency of $l^{\mathrm{Tx/Rx}}$ and θ^{Rx} to $\boldsymbol{r}^{\mathrm{w}}$, omitted here for conciseness. Furthermore, the additional term appearing in the definition of l^{Rx} compared to l^{Tx} stems from the change of variable (6) applied to the integral.

We assume the additional hypothesis

$$\cos\left(\frac{\theta^{\mathrm{Tx}} - \theta^{\mathrm{Rx}}}{2}\right) \approx 1, \tag{10}$$

which holds as long as both Tx and Rx angles remain close to 0. Equation (8) can then be rewritten as

$$\gamma^{\mathrm{DAS}}(\theta^{\mathrm{Tx}}, \boldsymbol{r}') \approx \int_{\theta^{\mathrm{Rx}}} s\left(\theta^{\mathrm{Tx}}, \theta^{\mathrm{Rx}}, \left\langle \boldsymbol{u}\left(\frac{\theta^{\mathrm{Tx}} + \theta^{\mathrm{Rx}}}{2}\right), \boldsymbol{r}' - \boldsymbol{r}^{\mathrm{w}}\right\rangle\right) \mathrm{d}\theta^{\mathrm{Rx}} \tag{11}$$

with

$$s(\theta^{\mathrm{Tx}}, \theta^{\mathrm{Rx}}, d) = l^{\mathrm{Tx}}(\theta^{\mathrm{Tx}}) l^{\mathrm{Rx}}(\theta^{\mathrm{Rx}}) f\left(\frac{\theta^{\mathrm{Tx}} + \theta^{\mathrm{Rx}}}{2}, d\right) \tag{12}$$

and

$$f(\theta, d) = \int_{\alpha^{\parallel}} v_{\mathrm{pe}}\left(\frac{2}{c_0}(d - \alpha^{\parallel})\right) \\ \int_{\alpha^{\perp}} \gamma\left(\alpha^{\parallel}\boldsymbol{u}(\theta) + \alpha^{\perp}\boldsymbol{u}^{\perp}(\theta) + \boldsymbol{r}^{\mathrm{w}}\right) \mathrm{d}\alpha^{\perp}\, \mathrm{d}\alpha^{\parallel}, \tag{13}$$

with $\boldsymbol{u}^{\perp}$ a vector perpendicular to $\boldsymbol{u}$ and d a variable representing the spatial displacement with respect to $\boldsymbol{r}^{\mathrm{w}}$.

According to (12), the series of sinograms s is given by the product the two aberration/apodization functions $l^{\mathrm{Tx/Rx}}$ with a function f, a term factoring in the reflectivity and the pulse-echo waveform. In fact, function f represents the local Radon transform of an unapodized image free of aberrations.

Therefore, our proposition for an adaptive beamforming method can be summarized as follows. We reconstruct using DAS a series γ^{DAS} of one image per insonification. These images are divided into zones (or patches) $\mathbb{V}(\boldsymbol{r}^{\mathrm{w}})$ to abide by the strong hypotheses introduced in this section. For each zone $\mathbb{V}(\boldsymbol{r}^{\mathrm{w}})$ we estimate first function s, then function f. Ultimately, function f is used to reconstruct an aberration-free image restricted to $\mathbb{V}(\boldsymbol{r}^{\mathrm{w}})$ and the local images obtained for different zones are combined into a single one.

TABLE I
TRANSDUCER AND SEQUENCE

Transducer	GE9L-D
Number of elements N^{el}	192
Pitch	230 µm
Aperture	43.93 mm
Element width	0.9·230 µm[a]
Element height	6 mm
Elevation focus	28 mm
Center frequency	5.3 MHz
Fractional bandwidth	75%
Steering angle spacing	5°
Number of insonifications N^{Tx}	9
Excitation cycles	1
Excitation frequency f_0	5.208 MHz
Sampling frequency f_{s}	20.833 MHz
Pulse repetition frequency	9 kHz

[a]No official data available, guessed value

III. METHOD

In this section, we present the practical aspects of the proposed method. We first detail the data acquisition and beamforming processes. We describe thereafter which patches $\mathbb{V}(\boldsymbol{r}^{\mathrm{w}})$ to select and how to obtain s for each patch, followed by the computation of f using tensor rank-1 decomposition. Finally, we present the reconstruction of the image, along with our implementation of the SVD beamformer used as a reference method.

A. Acquisition

All data considered throughout this article has been simulated or acquired using a GE9L-D ultrasound transducer (GE Healthcare, Chicago, Illinois, USA) connected to a Vantage 256 system (Verasonics, Kirkland, WA, USA). This transducer comprises a series of $N^{\mathrm{el}} = 192$ discrete sensors with positions x^{el}, $j = 1, ..., N^{\mathrm{el}}$ and we suppose it sends sequentially a series of discrete PWs with uniformly spaced steering angles θ_i^{Tx}, $i = 1, ..., N^{\mathrm{Tx}}$, with $N^{\mathrm{Tx}} = 9$ unless stated otherwise. The echoes signals are then recorded using all N^{el} elements. We directly apply the Hilbert transform to the raw measurements so that they can be described by a series of analytic signals gathered into a vector $\boldsymbol{m} \in \mathbb{C}^{N^{\mathrm{Tx}} N^{\mathrm{el}} N^{\mathrm{t}}}$. N^{t} denotes here the number of time samples considered after sampling with frequency f_{s}. The specifications of the transducer and sequence are summarized in Table I.

B. Delay-and-Sum

Given the measurements $\boldsymbol{m}$, we use DAS to compute the beamformed PW images γ^{DAS}. In practice, we discretize (5) as a sum over all sensors x^{el} and we interpolate cubically between time samples. Function γ^{DAS} is estimated at a series of points

$\boldsymbol{r}' = [x'_m, z'_n]^T,\ m = 1, ..., N^x,\ n = 1, ..., N^z$. Therefore, it is represented by a vector $\boldsymbol{\gamma}^{\mathrm{DAS}} \in \mathbb{C}^{N^{\mathrm{Tx}} N^x N^z}$.

To ease the implementation of the proposed method, we use an isotropic grid with a spatial spacing selected to guarantee a 200% fractional bandwidth $\Delta x' = \Delta z' = c_0/(8 f_0) = 38.5\,\mu\mathrm{m}$. The Tx apodization a^{Tx} is set to 1 whereas a Tukey apodization with 42° half-aperture and 0.15 cosine fraction is used as the Rx apodization a^{Rx} to reduce grating lobe level.

The 42° half-aperture is chosen to ensure that the directivity of an element reaches 6dB below its maximum value. Assuming a soft baffle boundary condition, we compute the theoretical angular directivity of a narrow element in the far field according to [30].

C. Windowed Radon Transform

As detailed in Section II-B, beamformed images γ^{DAS} must be restricted to a series of patches $\mathbb{V}(\boldsymbol{r}^{\mathrm{w}})$. Practically, we thus window γ^{DAS} with a function w shifted by a series of vectors $\boldsymbol{r}^{\mathrm{w}}$, such that $\boldsymbol{r}^{\mathrm{w}}$ represents the center of the window and $\mathbb{V}(\boldsymbol{r}^{\mathrm{w}}) = \left\{\boldsymbol{r}' :\ w\left(\boldsymbol{r}' - \boldsymbol{r}^{\mathrm{w}}\right) > 0\right\}$.

To estimate function s for a specific window position $\boldsymbol{r}^{\mathrm{w}}$, we can insert the windowing operation into (11). The result can be rewritten as

$$w\left(\cdot - \boldsymbol{r}^{\mathrm{w}}\right) \gamma^{\mathrm{DAS}} = \mathcal{R}^* s, \tag{14}$$

where $\mathcal{R}^*$ denotes the adjoint of the Radon transform, often designated as *backprojection*.

The inverse of the Radon transform is given by filtered backprojection, namely the composition of a filtering operator $\mathcal{F}$ and the adjoint of the Radon transform $\mathcal{R}^*$ [31]. Equation (14) can thus be further re-expressed as

$$s = \mathcal{F}^{-1}\mathcal{R}\left[w\left(\cdot - \boldsymbol{r}^{\mathrm{w}}\right)\gamma^{\mathrm{DAS}}\right]. \tag{15}$$

We define the inverse filtering operator $\mathcal{F}^{-1}$ applied to an arbitrary signal $g(d)$ as

$$\mathcal{F}^{-1}\left\{\hat{g}\right\}(\zeta) = \frac{1}{|\zeta|}\hat{g}(\zeta) \tag{16}$$

in the frequency domain, with $\hat{g}$ the Fourier transform of g and ζ the spatial frequency associated with d.

Equation (15) without the inverse filtering operation is known as a *windowed Radon transform* [32]. In the continuous domain, it can be written as

$$\tilde{s}\left(\theta^{\mathrm{Tx}}, \theta^{\mathrm{Rx}}, d, \boldsymbol{r}^{\mathrm{w}}\right) = \int_{\boldsymbol{r}'} \gamma^{\mathrm{DAS}}\left(\theta^{\mathrm{Tx}}, \boldsymbol{r}'\right) w\left(\boldsymbol{r}' - \boldsymbol{r}^{\mathrm{w}}\right) \delta\left(\left\langle \boldsymbol{u}\left(-\tfrac{\theta^{\mathrm{Tx}}+\theta^{\mathrm{Rx}}}{2}\right), \boldsymbol{r}' - \boldsymbol{r}^{\mathrm{w}}\right\rangle - d\right) \mathrm{d}\boldsymbol{r}'. \tag{17}$$

In practice, we consider N^{Rx} discrete angles θ^{Rx}_j, $j = 1, ..., N^{\mathrm{Rx}}$ and N^d values of d such that the spatial spacing of d is equal to the spatial grid spacing of the image $\Delta x' = \Delta z'$. Furthermore, we consider a discrete grid of window centers $\boldsymbol{r}^{\mathrm{w}}_{q,p}$ such that $p = 1, ..., N^{\mathrm{w},x}, q = 1, ..., N^{\mathrm{w},z}$, with $N^{\mathrm{w},x}$, $N^{\mathrm{w},z}$ the number of points in the x and z directions. The distance between two window centers is set to $\Delta x^{\mathrm{w}} = \Delta z^{\mathrm{w}} = 24\Delta x = 0.924\,\mathrm{mm}$ to ensure a sufficient overlap between windows since it is necessary in the image reconstruction step—c.f. Section III-E—. One can now apply the inverse filtering introduced in (16) to recover a *bona fide* estimation of s from $\tilde{s}$. Effectively, (16) is implemented as a linear system of equations in the spatial domain.

It is important to mention that the mathematical analysis detailed in Section II-B neglects the windowing of the image introduced in (17). A side effect of the windowing is the limitation of the angular resolution of s with respect to θ^{Rx} due to the convolution in the frequency domain between the the 2D spectrum of the window and the spectra of the images γ^{DAS}. To minimize this phenomenon, one must choose a window w with a narrow main lobe. Furthermore, the window must have a smooth profile to avoid artifacts in the reconstruction—c.f. Section III-E—. Thus, a Tukey window with 0.5 cosine fraction is chosen as a trade-off. The radius R^{w} must also achieve a critical trade-off. It needs to be sufficiently small to enforce the hypotheses introduced in Section II-B, but large enough to be resilient to local TRF variations. We determined empirically that $R^{\mathrm{w}} = 2\,\mathrm{mm}$ provides a good compromise for the proposed imaging configuration.

In turn, the Rx angular spacing is constrained by the size of the window. This constraint stems from the necessity to sample the whole 2D frequency plane. If this condition is not met, strong local grating lobe artefacts can appear in the reconstructed image. Let us recall that the main lobe width of a 2D Tukey window with radius R^{w} and 0.5 cosine fraction is $f^{\mathrm{w}} = 0.902/R^{\mathrm{w}}$. We posit that the distance between two samples in the frequency plane must be at most equal to the window main lobe width. In accordance with the size of the image grid, we need to guarantee a 200% fractional bandwith. Therefore, the maximum 2D spatial frequency magnitude we must consider is $f^{\max} = 2 \cdot 2f_0/c_0$. Under a small angle hypothesis, the minimum angular spacing of the Radon angle is then given by $f^{\mathrm{w}}/f^{\max} = 0.033 = 1.91°$. According to (17), there is a one-half factor between the Radon angle and the Rx angle, the maximum Rx angular spacing is consequently 3.82°. Regarding the maximum Rx angle, we set it such that it corresponds to the last angle not affected by the Rx apodization a^{Rx}, namely $0.85 \cdot 42° \approx 35°$.

D. Tensor Rank-1 Decomposition

To recover $l^{\mathrm{Tx/Rx}}$ and f from s, we propose to solve the following inverse problem

$$\min_{f, l^{\mathrm{Tx}}, l^{\mathrm{Rx}}} \frac{1}{2}\left\| l^{\mathrm{Tx}} l^{\mathrm{Rx}} f^{\mathrm{Tx,Rx}} - s\right\|^2_{\Omega^{\mathrm{Tx}}\times\Omega^{\mathrm{Rx}}\times\Omega^d} + \frac{\mu}{2}\left\|l^{\mathrm{Tx}}\right\|^2_{\Omega^{\mathrm{Tx}}}\left\|l^{\mathrm{Rx}}\right\|^2_{\Omega^{\mathrm{Rx}}}\left\|f\right\|^2_{\Omega^\theta\times\Omega^d}, \tag{18}$$

with

$$\left\|l^{\mathrm{Tx/Rx}}\right\|^2_{\Omega^{\mathrm{Tx/Rx}}} = \int_{\theta^{\mathrm{Tx/Rx}}\in\Omega^{\mathrm{Tx/Rx}}} \left|l^{\mathrm{Tx/Rx}}\left(\theta^{\mathrm{Tx/Rx}}\right)\right|^2 \mathrm{d}\theta^{\mathrm{Tx/Rx}}, \tag{19}$$

$$\left\|f\right\|^2_{\Omega^\theta\times\Omega^d} = \iint_{\theta\in\Omega^\theta, d\in\Omega^d} \left|f\left(\theta, d\right)\right|^2 \mathrm{d}\theta\,\mathrm{d}d, \tag{20}$$

$$\left\|g\right\|^2_{\Omega^{\mathrm{Tx}}\times\Omega^{\mathrm{Rx}}\times\Omega^d} = \iiint_{\theta^{\mathrm{Tx}}\in\Omega^{\mathrm{Tx}}, \theta^{\mathrm{Rx}}\in\Omega^{\mathrm{Rx}}, d\in\Omega^d} \left|g\left(\theta^{\mathrm{Tx}}, \theta^{\mathrm{Rx}}, d\right)\right|^2 \mathrm{d}\theta^{\mathrm{Tx}}\,\mathrm{d}\theta^{\mathrm{Rx}}\,\mathrm{d}d, \tag{21}$$

and

$$f^{\mathrm{Tx,Rx}}\left(\theta^{\mathrm{Tx}},\theta^{\mathrm{Rx}},d\right)=f\left(\frac{\theta^{\mathrm{Tx}}+\theta^{\mathrm{Rx}}}{2},d\right). \tag{22}$$

In (18), $\Omega^{\mathrm{Tx/Rx}}$, Ω^{θ}, and Ω^{d} denote the ranges of $\theta^{\mathrm{Tx/Rx}}$, θ, and d, respectively. Problem (18) can be interpreted as a weighted and regularized rank-1 canonical polyadic (CP) decomposition in the continuous domain.

The regularization term is necessary to prevent a divergence of the solution, for instance if l^{Tx} and l^{Rx} are null for certain angles. In fact, the regularization term enables a dynamical apodization of the image. A small regularization parameter μ implies that the proposed method compensates for the angular directivity of the sensors, among other magnitude effects acting on the received signals. Lateral resolution is thus typically favored at the expense of robustness to multiple scattering and diffraction artifacts. The opposite phenomenon occurs when a large regularization parameter μ is chosen. The proposed method is then more robust to artefacts at the expense of lateral resolution. We determined empirically that $\mu = 1$ provides a good trade-off—c.f. Section IV-B—. The adaptive apodization of the proposed method extends in effect the Tx adaptive apodization already enforced by SVD beamforming. This adaptive apodization can induce a gain of performance—especially contrast—compared to coherent compounding, even in the absence of aberrations.

We solve (18) with alternating least-squares (ALS), a common method for CP decomposition [33]. Its fundamental principle is to solve least-squares problems by fixing alternatively two out of the three variables f, l^{Tx}, and l^{Rx}. The ALS scheme with continuous signals is detailed in Algorithm 1, where $\bar{\cdot}$ denotes the complex conjugate. To the best of our knowledge, there exists no proof of convergence for ALS in the present case of weighted CP decomposition. Convergence guarantees exist however for the unweighted regularized case [33]. Even if we are not certain that ALS converges to a global minimum, we are guaranteed that it will converge to a local minimum that is at least as good—with respect to the loss—as the case where l^{Tx} and l^{Rx} are uniform.

In practice, we need to discretize l^{Tx}, l^{Rx}, and f. First of all, we can naturally express l^{Tx} as a vector $\boldsymbol{l}^{\mathrm{Tx}} \in \mathbb{C}^{N^{\mathrm{Tx}}}$. In addition, we can determine the discrete Rx angles $\boldsymbol{\theta}^{\mathrm{Rx}}$ and Radon angles $\boldsymbol{\theta}$ such that interpolation can be avoided in the implementation of Algorithm 1. To do so, the Tx and Rx angular spacings should be multiples of one another and the angular spacing of $\boldsymbol{\theta}$ should be half of the minimum of the Tx and Rx angular spacings. Consequently, we can infer that $\boldsymbol{\theta}^{\mathrm{Rx}} = [-35°, -32.5°, ..., 35°]$ since it must comply with criteria introduced in Section III-C, and that $\boldsymbol{\theta} = [-27.5°, -26.25°, ..., 27.5°]$ since the maximum mid-angle is given by $(35°+20°)/2 = 27.5°$. Practically, only a few iterations are necessary in order for ALS to converge, in particular we set N^{iter}=20.

Ultimately, Algorithm 1 is run for each window position $\boldsymbol{r}^{\mathrm{w}}_{p,q}$. Moreover, we normalize $\boldsymbol{l}^{\mathrm{Rx}}$ and $\boldsymbol{l}^{\mathrm{Tx}}$ and reweight $\boldsymbol{f}$ accordingly, ensuring a consistent amplitude of $\boldsymbol{f}$ between the different window positions.

Algorithm 1: Alternating Least Squares

Initialize uniformly l^{Tx};
Initialize uniformly l^{Rx};
for $i := 1$ *to* N^{iter} **do**

$$f(\theta,d) \leftarrow \frac{2\int_{\theta^{\mathrm{Tx}}} \bar{l}^{\mathrm{Tx}}\left(\theta^{\mathrm{Tx}}\right)\bar{l}^{\mathrm{Rx}}\left(2\theta-\theta^{\mathrm{Tx}}\right)s\left(\theta^{\mathrm{Tx}},2\theta-\theta^{\mathrm{Tx}},d\right)\mathrm{d}\theta^{\mathrm{Tx}}}{2\int_{\theta^{\mathrm{Tx}}}\left|l^{\mathrm{Tx}}\left(\theta^{\mathrm{Tx}}\right)l^{\mathrm{Rx}}\left(2\theta-\theta^{\mathrm{Tx}}\right)\right|^2\mathrm{d}\theta^{\mathrm{Tx}}+\mu\left\|l^{\mathrm{Tx}}\right\|^2_{\Omega^{\mathrm{Tx}}}\left\|l^{\mathrm{Rx}}\right\|^2_{\Omega^{\mathrm{Rx}}}};$$

$$l^{\mathrm{Tx}}\left(\theta^{\mathrm{Tx}}\right) \leftarrow \frac{\iint_{\theta^{\mathrm{Rx}},d}\bar{f}\left(\frac{\theta^{\mathrm{Tx}}+\theta^{\mathrm{Rx}}}{2},d\right)\bar{l}^{\mathrm{Rx}}\left(\theta^{\mathrm{Rx}}\right)s\left(\theta^{\mathrm{Tx}},\theta^{\mathrm{Rx}},d\right)\mathrm{d}\theta^{\mathrm{Rx}}\,\mathrm{d}d}{\iint_{\theta^{\mathrm{Rx}},d}\left|f\left(\frac{\theta^{\mathrm{Tx}}+\theta^{\mathrm{Rx}}}{2},d\right)l^{\mathrm{Rx}}\left(\theta^{\mathrm{Rx}}\right)\right|^2\mathrm{d}\theta^{\mathrm{Rx}}\,\mathrm{d}d+\mu\left\|l^{\mathrm{Rx}}\right\|^2_{\Omega^{\mathrm{Rx}}}\left\|f\right\|^2_{\Omega^{\theta}\times\Omega^{d}}};$$

$$l^{\mathrm{Rx}}\left(\theta^{\mathrm{Rx}}\right) \leftarrow \frac{\iint_{\theta^{\mathrm{Tx}},d}\bar{f}\left(\frac{\theta^{\mathrm{Tx}}+\theta^{\mathrm{Rx}}}{2},d\right)\bar{l}^{\mathrm{Tx}}\left(\theta^{\mathrm{Tx}}\right)s\left(\theta^{\mathrm{Tx}},\theta^{\mathrm{Rx}},d\right)\mathrm{d}\theta^{\mathrm{Tx}}\,\mathrm{d}d}{\iint_{\theta^{\mathrm{Tx}},d}\left|f\left(\frac{\theta^{\mathrm{Tx}}+\theta^{\mathrm{Rx}}}{2},d\right)l^{\mathrm{Tx}}\left(\theta^{\mathrm{Tx}}\right)\right|^2\mathrm{d}\theta^{\mathrm{Tx}}\,\mathrm{d}d+\mu\left\|l^{\mathrm{Tx}}\right\|^2_{\Omega^{\mathrm{Tx}}}\left\|f\right\|^2_{\Omega^{\theta}\times\Omega^{d}}};$$

end
Return: f, l^{Tx}, l^{Rx}

E. Image Reconstruction

Once a single sinogram f per window position is obtained using Algorithm 1, we recover the estimations of the corresponding local patches by applying the backprojection operator $\mathcal{R}^*$ to f

$$\gamma^{\mathrm{f,\,p}}\left(\boldsymbol{r}',\boldsymbol{r}^{\mathrm{w}}\right)=\int_{\theta} f\left(\theta,\left\langle\boldsymbol{u}(\theta),\boldsymbol{r}'-\boldsymbol{r}^{\mathrm{w}}\right\rangle,\boldsymbol{r}^{\mathrm{w}}\right)\mathrm{d}\theta, \tag{23}$$

in the continuous domain. Backprojection is then repeated for each window position $\boldsymbol{r}^{\mathrm{w}}_{p,q}$.

We need to reassemble the patches obtained with (23) into a single image γ^{f}. Unfortunately, each value of f is recovered up to a arbitrary phase. We must therefore make sure that the patches are added up in phase, otherwise detrimental artifacts are likely to appear. We thus perform the image reconstruction using Algorithm 2, where patches are added to the image γ^{f} after a phase correction v that is updated $N^{\mathrm{iter,\,out}}$ times. $N^{\mathrm{iter,\,out}}$ is set to 10 in practice. Moreover, we compute a normalization factor n to correct for magnitude variations induced by the windowing. The corrected image γ^{f} is discretized as a vector $\boldsymbol{\gamma}^{\mathrm{f}} \in \mathbb{C}^{N^x N^z}$, using the same grid than the initial images $\boldsymbol{\gamma}^{\mathrm{DAS}}$. The brightness (B)-mode image is ultimately computed as

$$\gamma^{\mathrm{f,\,B}}\left(\boldsymbol{r}'\right)=20\log_{10}\left|\gamma^{\mathrm{f}}\left(\boldsymbol{r}'\right)\right|. \tag{24}$$

F. SVD Beamforming

To compare the performance of our approach to a state-of-the art method, the SVD beamformer proposed in [20] is implemented. The implementation is performed as follows. First, we define w^{SVD} as a square window, such that the multiplication of an image with w^{SVD} shifted by $\boldsymbol{r}^{w}$ corresponds to a patch extraction. Consequently, we can solve the following

Algorithm 2: Image Reconstruction

$\gamma^{\mathrm{f}}(\boldsymbol{r}') \leftarrow 0$;
$n(\boldsymbol{r}') \leftarrow 0$;
for $p := 1$ *to* $N^{w,x}$ *and* $q := 1$ *to* $N^{w,z}$ **do**
  $\gamma^{\mathrm{f,\,w}}(\boldsymbol{r}', \boldsymbol{r}^{\mathrm{w}}_{p,q}) \leftarrow w(\boldsymbol{r}' - \boldsymbol{r}^{\mathrm{w}}_{p,q})\gamma^{\mathrm{f,\,p}}(\boldsymbol{r}', \boldsymbol{r}^{\mathrm{w}}_{p,q})$;
  $n(\boldsymbol{r}') \leftarrow n(\boldsymbol{r}') + w^2(\boldsymbol{r}' - \boldsymbol{r}^{\mathrm{w}}_{p,q})$;
  $\gamma^{\mathrm{f}}(\boldsymbol{r}') \leftarrow \gamma^{\mathrm{f}}(\boldsymbol{r}') + \gamma^{\mathrm{f,\,w}}(\boldsymbol{r}', \boldsymbol{r}^{\mathrm{w}}_{p,q})$;
end
for $i := 1$ *to* $N^{iter,\,out}$ **do**
  for $p := 1$ *to* $N^{w,x}$ *and* $q := 1$ *to* $N^{w,z}$ **do**
    $\gamma^{\mathrm{f},0}(\boldsymbol{r}') \leftarrow \gamma^{\mathrm{f}}(\boldsymbol{r}') - \gamma^{\mathrm{f,\,w}}(\boldsymbol{r}', \boldsymbol{r}^{\mathrm{w}}_{p,q})$;
    $v \leftarrow \int_{\boldsymbol{r}'} \gamma^{\mathrm{f},0}(\boldsymbol{r}')\bar{\gamma}^{\mathrm{f,\,w}}(\boldsymbol{r}', \boldsymbol{r}^{\mathrm{w}}_{p,q})\,\mathrm{d}\boldsymbol{r}'$;
    $\gamma^{\mathrm{f,\,w}}(\boldsymbol{r}') \leftarrow \frac{v}{|v|}\gamma^{\mathrm{f,\,w}}(\boldsymbol{r}')$;
  end
  $\gamma^{\mathrm{f}}(\boldsymbol{r}') \leftarrow 0$;
  for $p := 1$ *to* $N^{w,x}$ *and* $q := 1$ *to* $N^{w,z}$ **do**
    $\gamma^{\mathrm{f}}(\boldsymbol{r}') \leftarrow \gamma^{\mathrm{f}}(\boldsymbol{r}') + \gamma^{\mathrm{f,\,w}}(\boldsymbol{r}', \boldsymbol{r}^{\mathrm{w}}_{p,q})$;
  end
end
$\gamma^{\mathrm{f}}(\boldsymbol{r}') = \frac{\gamma^{\mathrm{f}}(\boldsymbol{r}')}{n(\boldsymbol{r}')}$;
Return: γ^{f}

inverse problem

$$\underset{\gamma^{\mathrm{f,\,p}},\,\|l^{\mathrm{Tx}}\|=1}{\arg\min} \int_{\boldsymbol{r}'}\int_{\theta^{\mathrm{Tx}}} \left|\gamma^{\mathrm{f,\,p}}(\boldsymbol{r}')l^{\mathrm{Tx}}(\theta^{\mathrm{Tx}}) - \gamma^{\mathrm{DAS}}(\theta^{\mathrm{Tx}}, \boldsymbol{r}')w^{\mathrm{SVD}}(\boldsymbol{r}' - \boldsymbol{r}^{w})\right|^2 \mathrm{d}\theta^{\mathrm{Tx}}\,\mathrm{d}\boldsymbol{r}', \quad (25)$$

for all the patch positions $\boldsymbol{r}^{w}$. This problem results in a function $\gamma^{\mathrm{f,\,p}}(\boldsymbol{r}', \boldsymbol{r}^{w})$ that can be directly used by Algorithm 2 with $w = w^{\mathrm{SVD}}$ to reconstruct the corrected image γ^{f}. Similarly to the proposed method, γ^{DAS}, $\gamma^{\mathrm{f,\,p}}$ and l^{Tx} can be represented by discrete complex vectors. The solution of (25) is thus given by the two leading singular vectors of the windowed series of images expressed as a matrix.

We set the parameters of the SVD beamformer to be as close as possible to the ones of the proposed method to ensure a meaningful comparison. In particular the half-side of a square patch is identical to the window radius R^{w} (2 mm) and the same distance between patch centers is kept.

IV. Experiments

In this section, we detail the experiments we perform to check the validity of the proposed method and present their results. We also compare our method to standard coherent compounding and SVD beamforming. We first assess quantitatively the proposed method using simulated data, followed by a test of the method with in-vivo data.

A. Simulation

We depict in Figure 1a, the numerical phantom designed to quantitatively assess the performance of our method. A SoS of 1540 m s^{-1} is set in the phantom background. Two inclusions—one anechoic and one hypoechoic 6dB below the background echogeneicity—and six scatterers are embedded within the medium. Moreover, we add an irregular aberrating layer with a SoS of 1500 m s^{-1} and an echogeneicity 6dB above the background on top of the phantom. We choose such a layer—in opposition to a flat layer or a phase screen—for its capacity to generate complex phase aberrations with strong lateral variations. Complex laterally-varying aberrations can typically occur in the imaging of the abdominal wall due to the interweave of muscle and fat tissues. We simulated using k-Wave [34] the data corresponding to 10 different speckle realisations of the phantom.

In addition, figure 1a presents the zones considered to evaluate the performance of our method. As detailed bellow, three different key features have been analyzed: contrast, scatterer resolution and the ability to accurately correct aberrations.

- To compare contrast, we compute the contrast ratio (CR) between the two inclusions and their adjacent backgrounds. The inclusions' interiors used to estimate the CRs are highlighted with purple and green lines and the backgrounds are bounded by lighter lines. To account for the apparent position displacement due to the aberrating layer, the centers of both inclusions are shifted by 200 µm along the z-axis in the coherent compounding, SVD beamforming and proposed method cases.
- To compare resolution, we compute the axial and lateral full width at half maximum (FWHM) of near and far field scatterers. They are displayed in red and orange in Figure 1a, respectively.
- Lastly, we check whether the proposed method is able to correctly compensate for Tx and Rx aberrations and recover speckle patterns coherent with a theoretical unaberrated image. To do so, we generate a reference image with DAS and coherent compounding from a simulation without the top aberrating layer. We then compute the maximum of the normalized cross-correlation between a series of patches extracted from the target CRF image and the corresponding patch of the reference CRF aberration-free image. The patches selected to perform this analysis present speckle patterns that are especially aberrated in the coherent compounding images. These patches are displayed in blue in Figure 1a.

Figures 1b-1d show the results of coherent compounding, SVD beamforming and the proposed method using data from a single speckle realisation of the phantom. Close-ups of a near-field and a far-field scatterers (in red and orange in figure 1a) are also presented on the bottom row. Figure 1e displays the reference aberration-free image. Furthermore, we summarize on Table II the metrics computed on the phantom, averaged over 10 speckle realisations. The standard deviation is given between parentheses.

From the results presented in Table II, we can observe that the most noticeable benefit of the proposed method with respect to coherent compounding and SVD beamforming is its capacity to accurately reconstruct the scatterers. As depicted in the close-ups of Figure 1, the SVD beamformer improves the quality of the far-field scatterer—even if it is not reflected on

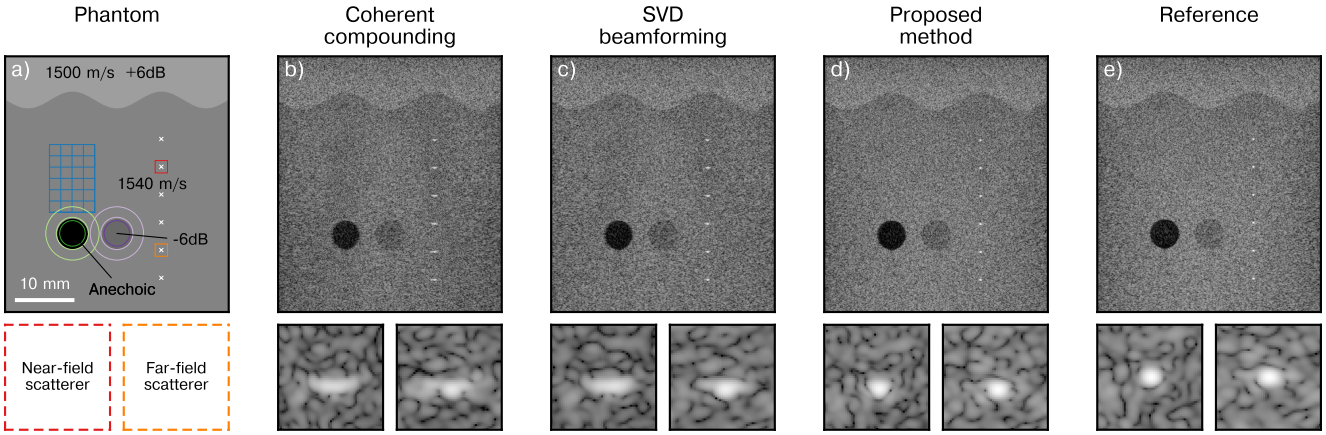

Fig. 1. Top row: B-mode images reconstructed from simulated data, bottom row: examples of reconstructed scatterers. a) Phantom geometry with the top aberrating layer and the zones considered for the computation of the metrics highlighted. b) Coherent compounding image reconstruced from a single speckle realisation of the phantom. c) Result of the SVD beamformer. d) Result of the proposed method. e) Reference coherent compounding image obtained from data simulated without the aberrating layer.

TABLE II
SIMULATION RESULTS

	Coherent compounding	SVD beamforming	Proposed method	Reference
Anechoic CR [dB]	-18.83 (0.33)	-22.08 (0.39)	-25.08 (0.36)	-22.95 (0.36)
Hypoechoic CR[a] [dB]	-5.86 (0.23)	-6.12 (0.33)	-6.29 (0.26)	-6.04 (0.27)
Near-field lateral FWHM [μm]	594 (29)	641 (28)	247 (4)	244 (2)
Near-field axial FWHM [μm]	199 (3)	200 (6)	211 (4)	210 (4)
Far-field lateral FWHM [μm]	333 (19)	333 (10)	260 (6)	280 (6)
Far-field axial FWHM [μm]	220 (3)	218 (3)	204 (3)	206 (4)
Normalized cross-correlation	0.768 (0.085)	0.796 (0.072)	0.951 (0.027)	×[b]

[a]Target value: -6dB
[b]The cross-correlation is computed with respect to the reference image

its lateral FWHM—but fails to correct the near-field scatterer. On the contrary, the proposed method recovers scatterers that are qualitatively and quantitatively comparable to the ones of the reference image. Nevertheless, we can notice that the axial displacement in the apparent positions of the scatterers compared to the reference image is not compensated by the SVD beamforming and the proposed method.

Regarding the anechoic inclusion, we can notice that both SVD beamforming and the proposed method provide contrast improvements compared to coherent compounding. The proposed method achieves however a better contrast ratio—even outperforming the contrast ratio of the reference image—and a better reconstruction of the inclusion's shape. With regard to the hypoehoic inclusion, all four methods achieve similar average contrast ratios with similar standard deviations.

Finally, from the normalized cross-correlation with the reference image, we observe that our method highly outperforms the SVD beamforming and the coherent compounding. The SVD beamforming only achieves a limited improvement compared to coherent compounding. In contrast, the image reconstructed using the proposed method consistently correlates with the reference image to a high degree, thus accurately compensating for aberrations and maintaining speckle coherence.

B. Regularization Parameter

One of the key enablers of our method is the regularization parameter. To quantify its impact on imaging quality, we reconstruct the images corresponding to the 10 speckle realizations of the phantom with different values of the regularization parameter μ. We present in Figure 2 the evolution of the metrics—at the exception of axial resolution of the scatterers which is only weakly affected by the aberrations, as seen in Table II—with respect to μ. We depict in the same figure the metrics associated with coherent compounding, SVD beamforming and the reference image, which are all independent from the regularization parameter. The plain lines and shaded areas represent the mean and standard deviation of the metrics over the 10 speckle realisations, respectively.

We can notice that the trade-off between resolution and robustness described in Section III-D is confirmed experimentally. Indeed, the lower the regularization parameter is, the smaller the lateral resolution becomes. The resolution of the reference image is even outperformed on both the near and far-field scatterers when $\mu < 1$. By contrast, the contrast ratios of the anechoic inclusion—and to a lesser degree the hypoechoic inclusion—increase, a sign that the proposed method becomes more sensible to diffraction artefacts. This sensibility to diffraction artefacts can also be observed on the normalized cross-correlation, since it also worsens when μ decreases. The change in cross-correlation cannot however be solely explained by the presence of artefacts since the speckle is tightened when μ decreases. For illustration, we depict on Figure 3 a scatterer and the anechoic inclusion for three values of μ, along with the reference image.

To conclude, we determine the default regularization parameter $\mu = 1$ as the value at which the lateral resolution

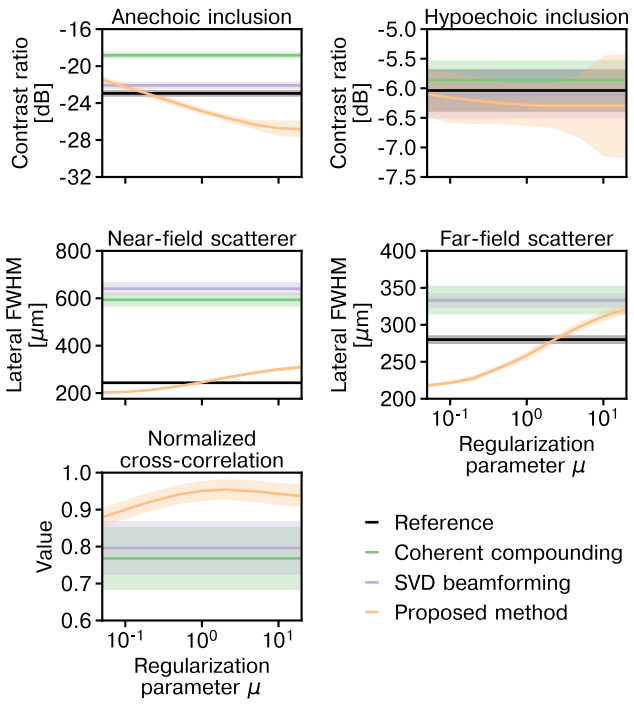

Fig. 2. Influence of the regularization parameter μ on the average image quality metrics. The metrics are computed over 10 speckle realizations of the phantom and depicted with their standard deviations.

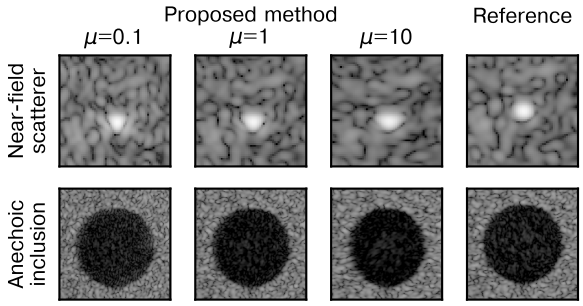

Fig. 3. B-mode examples of scatterer and anechoic inclusion reconstructed using different values of the regularization parameter μ. They are compared with a reference aberration-free image and displayed with a 60 dB dynamic range.

achieved by the proposed method is at least equal to the one of the reference image.

C. Number of Insonifications

We also test the influence of the number of insonifications on the quality of the image reconstruction. Figure 4 represents the contrasts and speckle correlation with respect to the number of PWs considered N^{PW}. The plain lines and shaded areas represent again the mean and standard deviation of the metrics over the 10 speckle realisations, respectively. The scatterers' FWHMs are omitted due to the limited influence of the amount of PWs. With regard to the proposed method, the number of Radon angles and Rx angles are updated for each N^{PW} to comply with the criteria disclosed in Section III-D.

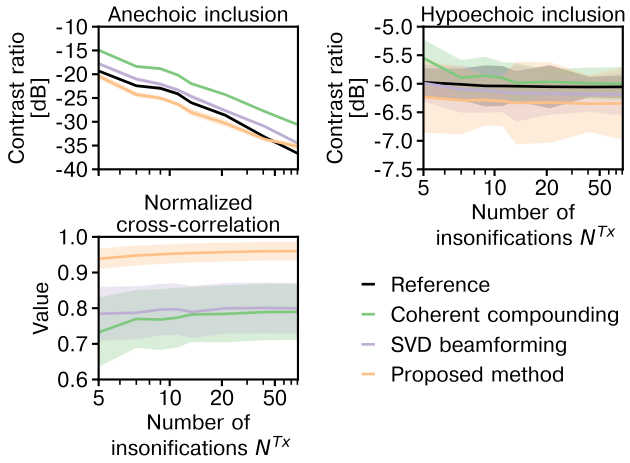

Fig. 4. Evolution of the average image quality metrics with respect to the number of insonifications. The metrics are computed over 10 speckle realizations of the phantom and depicted with their standard deviations.

From Figure 4, we can observe an improvement of the anechoic CR with the number of PWs, regardless of the method applied. Notably, the relative difference between the four cases stays approximately constant. A noteworthy exception occurs when $N^{\mathrm{Tx}} > 40$, the results of the proposed method become worse than the reference image. The influence of the number of PWs on the hypoechoic CR and speckle correlation is more limited. Nonetheless, an improved stability of the correlation with respect to N_{Tx} can be observed with SVD beamforming and the proposed method, especially when $N_{\mathrm{Tx}} < 10$. Overall, we can conclude that the proposed method does not require a specific range of PWs to be effective.

D. In-vivo

To assess the in-vivo performances of the proposed method, we acquired two sets of data on the abdominal wall of a healthy volunteer (27 years old male), using 9 PW insonifications. The ultrasound sequence has been approved for research with human subjects by the Cantonal Ethics Committee of the Canton of Vaud, Switzerland. We reconstruct the images with coherent compounding, SVD beamforming and the proposed method, for both scanning positions. The resulting B-mode images are depicted in Figure 5, along with close-up of four areas of interest.

We can notice in each image the complex structure of the medium, with a series of non-parallel muscle and fat layers. Those layers are likely to possess a different SoS than the expected $c_0 = 1540\,\mathrm{m\,s^{-1}}$ [7], and thus to generate aberrations.

We can first observe that the SVD beamformer and proposed method both improve contrast with respect to coherent compounding. The contrast improvement is especially visible in the median layer—between 2 and 3 cm—of both images and corroborates the results obtained with simulated data. However, the most noteworthy effect of the proposed method is its capacity to reconstruct scatterers. It can be observed in the top area of interest of the first image. An ovoidal scatterer is reconstructed, whereas it lacks definition with the two reference methods. It can also be seen in the bottom

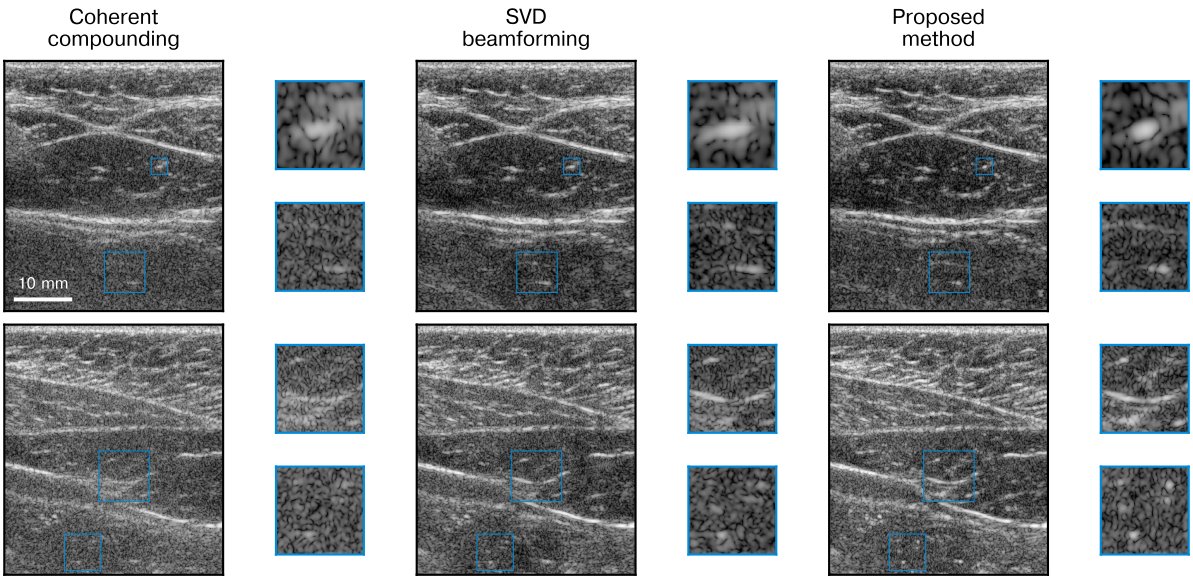

Fig. 5. Two in-vivo images of an abdominal wall (top and bottom row), using 9 plane wave insonifications and a 60 dB dynamic range. Results of coherent compounding, SVD beamforing and the proposed method are depicted. Areas of interest are highlighted in blue.

zone of interest of the second image. The proposed method reveals the presence of five scatterers whereas their presence can only be guessed from the two reference methods. Overall, our method permits a general qualitative improvement of the images. As an illustration, we can see in the top zone of interest of the second image the reconstruction of an interface, whereas it appears faint with coherent compounding or split in half with SVD beamforming.

V. Discussion

In this article, we introduce a novel adaptative beamforming method able to correct aberrations caused by SoS variations in the imaged medium. We show using simulated data that our method accurately corrects phase aberrations and recovers an image that correlates to a high degree with an ideal aberration-free image. In particular, the lateral resolution is greatly improved. We also establish that the proposed method allows a contrast improvement with respect to DAS even when aberration-free data are considered. Lastly, we present qualitative in-vivo results confirming, in particular, an improvement in scatterer resolution with regard to both coherent compounding and SVD beamforming.

As desired, our method is highly parallelizable. Specifically, the bulk of the proposed technique can be performed simultaneously for each patch. The windowed Radon transform—the most computationally heavy operation of our method—can be parallelized further with respect to the Tx angles. The main temporal bottleneck is then given by the two iterative algorithms (Algorithms 1 and 2), but the numbers of iterations N^{iter} and $N^{\text{iter, out}}$ remain small in practice. Our prototype GPU implementation using 9PWs currently runs in 30 seconds on an Nvidia GeForce 2080 Ti GPU (Nvidia Corporation, Santa Clara, CA, USA). However, the performance of the code can be significantly improved and the choice of parameters can be optimized with respect to the computation time. Overall, we are confident that the computation time can be reduced to allow real-time image reconstruction.

The proposed method posits that the Tx and Rx aberrations $l^{\text{Tx/Rx}}(\theta)$ are essentially different. If this fact holds true for their amplitude (9), their phases in the continuous domain are equal in theory. Therefore, adding a phase equality constraint —or a penalty on the phase difference—to $l^{\text{Tx/Rx}}(\theta)$ could in principle improve the quality of the estimation of f. In practice however, it would increase the computational complexity of Algorithm 1 and mitigate its convergence guarantees. Moreover, tissue movements may occur between insonifications. Such movements can be interpreted as Tx phase shifts. Considering separate Tx and Rx aberrations likely provides additional robustness to in-vivo movement artifacts, especially when the number of insonifications grows.

A fundamental limitation of the proposed method is its failure to retrieve the absolute position of reflective structures. This drawback arises from the estimation of time delays by phase shifts and from the inability of our method to recover the global phase of $\boldsymbol{l}^{\text{Tx/Rx}}$. A reconstruction of the SoS map is therefore probably necessary to address this shortcoming. The parallelizability of such a method would however be impaired. The phase-shift hypothesis also limits the maximum aberration delay our method can correct. The applicability of our method to cases where strong aberrations are present is therefore hindered.

Nonetheless, we can state that our method is, first of all, useful to improve B-mode imaging, as indicated by the in-vivo examples. The proposed method can be especially relevant to the challenging case of overweight patients, since the presence of fat is likely to generate SoS aberrations [7]. Due to the low number of insonifications required, our method can also be used in conjunction with portable transducers, since the amount of data they can acquire and transmit is likely to be limited. Moreover, SoS aberrations affect the quality of displacement tracking between consecutive frames.

The performances of methods such as shear-wave elastography are therefore diminished. Consequently, displacement-tracking-based techniques could benefit from the capacity of the proposed method to correct for Tx and Rx aberrations. Further research is however necessary to establish any positive effect of the proposed method.

ACKNOWLEDGMENT

The authors would like to thank Roser Vinals Terres for her re-reading, Baptiste Hériard-Dubreuil for his regular feedback, Thomas Deffieux for the helpful discussion, and Valentin Vuillon for his preliminary work on the method.

REFERENCES

[1] M. Tanter and M. Fink, "Ultrafast imaging in biomedical ultrasound," *IEEE Transactions on Ultrasonics, Ferroelectrics, and Frequency Control*, vol. 61, no. 1, pp. 102–119, Jan. 2014.

[2] G. Montaldo, M. Tanter, J. Bercoff, N. Benech, and M. Fink, "Coherent plane-wave compounding for very high frame rate ultrasonography and transient elastography," *IEEE transactions on ultrasonics, ferroelectrics, and frequency control*, vol. 56, no. 3, pp. 489–506, 2009.

[3] L. Sandrin, M. Tanter, S. Catheline, and M. Fink, "Shear modulus imaging with 2-d transient elastography," *IEEE transactions on ultrasonics, ferroelectrics, and frequency control*, vol. 49, no. 4, pp. 426–435, 2002.

[4] M. Tanter, J. Bercoff, L. Sandrin, and M. Fink, "Ultrafast compound imaging for 2-d motion vector estimation: Application to transient elastography," *IEEE transactions on ultrasonics, ferroelectrics, and frequency control*, vol. 49, no. 10, pp. 1363–1374, 2002.

[5] J.-L. Gennisson, T. Deffieux, M. Fink, and M. Tanter, "Ultrasound elastography: Principles and techniques," *Diagnostic and Interventional Imaging*, vol. 94, no. 5, pp. 487–495, May 2013.

[6] C. Demené, J. Robin, A. Dizeux, B. Heiles, M. Pernot, M. Tanter, and F. Perren, "Transcranial ultrafast ultrasound localization microscopy of brain vasculature in patients," *Nature biomedical engineering*, vol. 5, no. 3, pp. 219–228, 2021.

[7] S. A. Goss, R. L. Johnston, and F. Dunn, "Comprehensive compilation of empirical ultrasonic properties of mammalian tissues," *The Journal of the Acoustical Society of America*, vol. 64, no. 2, pp. 423–457, Aug. 1978.

[8] J. J. Dahl, M. S. Soo, and G. E. Trahey, "Spatial and temporal aberrator stability for real-time adaptive imaging," *IEEE transactions on ultrasonics, ferroelectrics, and frequency control*, vol. 52, no. 9, pp. 1504–1517, 2005.

[9] G. E. Trahey and S. W. Smith, "Properties of acoustical speckle in the presence of phase aberration part I: first order statistics," *Ultrasonic Imaging*, vol. 10, no. 1, pp. 12–28, 1988.

[10] G. C. Ng, S. S. Worrell, P. D. Freiburger, and G. E. Trahey, "A comparative evaluation of several algorithms for phase aberration correction," *IEEE transactions on ultrasonics, ferroelectrics, and frequency control*, vol. 41, no. 5, pp. 631–643, 1994.

[11] S. Flax and M. O'Donnell, "Phase-aberration correction using signals from point reflectors and diffuse scatterers: Basic principles," *IEEE transactions on ultrasonics, ferroelectrics, and frequency control*, vol. 35, no. 6, pp. 758–767, 1988.

[12] M. O'donnell and S. Flax, "Phase-aberration correction using signals from point reflectors and diffuse scatterers: Measurements," *IEEE transactions on ultrasonics, ferroelectrics, and frequency control*, vol. 35, no. 6, pp. 768–774, 1988.

[13] P. Stähli, M. Kuriakose, M. Frenz, and M. Jaeger, "Improved forward model for quantitative pulse-echo speed-of-sound imaging," *Ultrasonics*, vol. 108, p. 106168, Dec. 2020.

[14] P. Stahli, M. Frenz, and M. Jaeger, "Bayesian approach for a robust speed-of-sound reconstruction using pulse-echo ultrasound," *IEEE Transactions on Medical Imaging*, vol. 40, no. 2, pp. 457–467, Feb. 2021.

[15] M. Jaeger, G. Held, S. Peeters, S. Preisser, M. Grünig, and M. Frenz, "Computed Ultrasound Tomography in Echo Mode for Imaging Speed of Sound Using Pulse-Echo Sonography: Proof of Principle," *Ultrasound in Medicine & Biology*, vol. 41, no. 1, pp. 235–250, Jan. 2015.

[16] S. J. Sanabria, E. Ozkan, M. Rominger, and O. Goksel, "Spatial domain reconstruction for imaging speed-of-sound with pulse-echo ultrasound: simulation and *in vivo* study," *Physics in Medicine & Biology*, vol. 63, no. 21, p. 215015, Oct. 2018.

[17] R. Ali and J. J. Dahl, "Distributed phase aberration correction techniques based on local sound speed estimates," in *2018 IEEE International Ultrasonics Symposium (IUS)*. IEEE, 2018, pp. 1–4.

[18] R. Rau, D. Schweizer, V. Vishnevskiy, and O. Goksel, "Ultrasound aberration correction based on local speed-of-sound map estimation," in *2019 IEEE International Ultrasonics Symposium (IUS)*. IEEE, 2019, pp. 2003–2006.

[19] M. Jaeger, E. Robinson, H. G. Akarçay, and M. Frenz, "Full correction for spatially distributed speed-of-sound in echo ultrasound based on measuring aberration delays via transmit beam steering," *Physics in Medicine and Biology*, vol. 60, no. 11, pp. 4497–4515, Jun. 2015.

[20] H. Bendjador, T. Deffieux, and M. Tanter, "The SVD beamformer: Physical principles and application to ultrafast adaptive ultrasound," *IEEE Transactions on Medical Imaging*, vol. 39, no. 10, pp. 3100–3112, Oct. 2020.

[21] H. Bendjador, S. Décombas-Deschamps, M. D. Burgio, R. Sartoris, B. Van Beers, V. Vilgrain, T. Deffieux, and M. Tanter, "The SVD beamformer with diverging waves: a proof-of-concept for fast aberration correction," *Physics in Medicine & Biology*, vol. 66, no. 18, p. 18LT01, 2021.

[22] H. Bendjador, T. Deffieux, and M. Tanter, "SVD beamforming for ultrafast aberration correction and real-time speed-of-sound quantification," in *2020 IEEE International Ultrasonics Symposium (IUS)*. Las Vegas, NV, USA: IEEE, Sep. 2020, pp. 1–4.

[23] W. Lambert, J. Robin, L. A. Cobus, M. Fink, and A. Aubry, "Ultrasound matrix imaging. i. the focused reflection matrix, the f-factor and the role of multiple scattering." *IEEE Transactions on Medical Imaging*, 2022.

[24] W. Lambert, L. A. Cobus, J. Robin, M. Fink, and A. Aubry, "Ultrasound matrix imaging. ii. the distortion matrix for aberration correction over multiple isoplanatic patches." *IEEE Transactions on Medical Imaging*, 2022.

[25] G. Jansen, N. Awasthi, H.-M. Schwab, and R. Lopata, "Enhanced radon domain beamforming using deep-learning-based plane wave compounding," in *2021 IEEE International Ultrasonics Symposium (IUS)*, 2021, pp. 1–4.

[26] H.-M. Schwab, F. Van De Vosse, and R. Lopata, "An r-space theorem for plane wave ultrasound reconstruction," in *2020 IEEE International Ultrasonics Symposium (IUS)*. IEEE, 2020, pp. 1–4.

[27] J. A. Jensen, "A model for the propagation and scattering of ultrasound in tissue," *The Journal of the Acoustical Society of America*, vol. 89, no. 1, pp. 182–190, 1991.

[28] A. Besson, D. Perdios, F. Martinez, Z. Chen, R. E. Carrillo, M. Arditi, Y. Wiaux, and J.-P. Thiran, "Ultrafast Ultrasound Imaging as an Inverse Problem: Matrix-Free Sparse Image Reconstruction," *IEEE Transactions on Ultrasonics, Ferroelectrics, and Frequency Control*, vol. 65, no. 3, pp. 339–355, Mar. 2018.

[29] A. Besson, L. Roquette, D. Perdios, M. Simeoni, M. Arditi, P. Hurley, Y. Wiaux, and J.-P. Thiran, "A physical model of nonstationary blur in ultrasound imaging," *IEEE Transactions on Computational Imaging*, vol. 5, no. 3, pp. 381–394, 2019.

[30] A. Selfridge, G. Kino, and B. Khuri-Yakub, "A theory for the radiation pattern of a narrow-strip acoustic transducer," *Applied Physics Letters*, vol. 37, no. 1, pp. 35–36, 1980.

[31] S. Helgason, *The radon transform*. Springer, 1980, vol. 2.

[32] G. Kaiser and R. F. Streater, "Windowed radon transforms, analytic signals, and the wave equation," *Wavelets: A tutorial in theory and applications*, pp. 399–441, 1992.

[33] P. Comon, X. Luciani, and A. L. De Almeida, "Tensor decompositions, alternating least squares and other tales," *Journal of Chemometrics: A Journal of the Chemometrics Society*, vol. 23, no. 7-8, pp. 393–405, 2009.

[34] B. E. Treeby and B. T. Cox, "k-wave: Matlab toolbox for the simulation and reconstruction of photoacoustic wave fields," *Journal of biomedical optics*, vol. 15, no. 2, p. 021314, 2010.